General synthesis and structural evolution of a layered family of Ln8(OH)20Cl4 x nH2O (Ln = Nd, Sm, Eu, Gd, Tb, Dy, Ho, Er, Tm, and Y).

8 AUTHORS, INCLUDING:

Fengxia Geng
Soochow University (PRC)
35 PUBLICATIONS   **754** CITATIONS

SEE PROFILE

Yoshitaka Matsushita
National Institute for Materials Science
158 PUBLICATIONS   **2,061** CITATIONS

SEE PROFILE

General Synthesis and Structural Evolution of a Layered Family of Ln$_8$(OH)$_{20}$Cl$_4$·nH$_2$O (Ln = Nd, Sm, Eu, Gd, Tb, Dy, Ho, Er, Tm, and Y)

Fengxia Geng,[†,‡] Yoshitaka Matsushita,[§] Renzhi Ma,[†] Hao Xin,[†,‖]
Masahiko Tanaka,[§] Fujio Izumi,[⊥] Nobuo Iyi,[†] and Takayoshi Sasaki*,[†,‡]

International Center for Materials Nanoarchitectonics and Quantum Beamline Center, National Institute for Materials Science, 1-1 Namiki, Tsukuba, Ibaraki 305-0044, Graduate School of Pure and Applied Sciences, University of Tsukuba, 1-1-1 Tennodai, Tsukuba, Ibaraki 305-8571, and Beam Line Station, National Institute for Materials Science, 1-1-1 Kouto, Sayo-cho, Sayo-gun, Hyogo 679-5148, Japan

Received September 5, 2008; E-mail: SASAKI.Takayoshi@nims.go.jp

Abstract: The synthesis process and crystal structure evolution for a family of stoichiometric layered rare-earth hydroxides with general formula Ln$_8$(OH)$_{20}$Cl$_4$·nH$_2$O (Ln = Nd, Sm, Eu, Gd, Tb, Dy, Ho, Er, Tm, and Y; $n \approx 6-7$) are described. Synthesis was accomplished through homogeneous precipitation of LnCl$_3$·xH$_2$O with hexamethylenetetramine to yield a single-phase product for Sm–Er and Y. Some minor coexisting phases were observed for Nd^{3+} and Tm^{3+}, indicating a size limit for this layered series. Light lanthanides (Nd, Sm, Eu) crystallized into rectangular platelets, whereas platelets of heavy lanthanides from Gd tended to be of quasi-hexagonal morphology. Rietveld profile analysis revealed that all phases were isostructural in an orthorhombic layered structure featuring a positively charged layer, [Ln$_8$(OH)$_{20}$(H$_2$O)$_n$]$^{4+}$, and interlayer charge-balancing Cl$^-$ ions. In-plane lattice parameters a and b decreased nearly linearly with a decrease in the rare-earth cation size. The interlamellar distance, c, was almost constant ($\sim$8.70 Å) for rare-earth elements Nd^{3+}, Sm^{3+}, and Eu^{3+}, but it suddenly decreased to $\sim$8.45 Å for Tb^{3+}, Dy^{3+}, Ho^{3+}, and Er^{3+}, which can be ascribed to two different degrees of hydration. Nd^{3+} typically adopted a phase with high hydration, whereas a low-hydration phase was preferred for Tb^{3+}, Dy^{3+}, Ho^{3+}, Er^{3+}, and Tm^{3+}. Sm^{3+}, Eu^{3+}, and Gd^{3+} samples were sensitive to humidity conditions because high- and low-hydration phases were interconvertible at a critical humidity of 10%, 20%, and 50%, respectively, as supported by both X-ray diffraction and gravimetry as a function of the relative humidity. In the phase conversion process, interlayer expansion or contraction of $\sim$0.2 Å also occurred as a possible consequence of absorption/desorption of H$_2$O molecules. The hydration difference was also evidenced by refinement results. The number of coordinated water molecules per formula weight, n, changed from 6.6 for the high-hydration Gd sample to 6.0 for the low-hydration Gd sample. Also, the hydration number usually decreased with increasing atomic number; e.g., $n = 7.4, 6.3, 7.2$, and 6.6 for high-hydration Nd, Sm, Eu, and Gd, and $n = 6.0, 5.8, 5.6, 5.4$, and 4.9 for low-hydration Gd, Tb, Dy, Ho, and Er. The variation in the average Ln–O bond length with decreasing size of the lanthanide ions is also discussed. This family of layered lanthanide compounds highlights a novel chemistry of interplay between crystal structure stability and coordination geometry with water molecules.

Introduction

Layered rare-earth hydroxides containing pure lanthanide cations (Ln^{3+}) in the host layer, although largely overlooked, represent an intriguing new host–guest system that offers unique opportunities for engineering new multifunctional materials. The rigid organic anion-intercalated metal–organic framework of [R$_4$(OH)$_{10}$(H$_2$O)$_4$]$_n$A$_n$ (R = rare-earth ions Ho, Dy, Yb, and Y; A = intercalated organic anions 2,6-naphthalenedisulfonate

(NDS^{2-}) and 2,6-anthraquinonedisulfonate (AQDS^{2-})) was revealed to be a heterogeneous catalyst of high quality due to its high ability to vary the coordination number in the catalysis process.[1] Recently, we realized the first example of a large-size lanthanide Eu^{3+}-based layered hydroxide that has an orthorhombic layered structure comprising a positively charged layer of [Eu$_8$(OH)$_{20}$(H$_2$O)$_{6.4}$]$^{3+}$ and interlayer Cl$^-$ ions.[2] Since the interlayer Cl$^-$ ions were acting as counterions, they were found to be readily exchangeable for various anions (NO$_3^-$, SO$_4^{2-}$, dodecylsulfonate (DS$^-$), etc.). The material exhibits

† International Center for Materials Nanoarchitectonics, National Institute for Materials Science.
‡ University of Tsukuba.
§ Beam Line Station, National Institute for Materials Science.
‖ Present address: Department of Chemical Engineering, University of Washington, Seattle, WA 98195-1750.
⊥ Quantum Beamline Center, National Institute for Materials Science.

(1) Gándara, F.; Perles, J.; Snejko, N.; Iglesias, M.; Gómez-Lor, B.; Gutiérrez-Puebla, E.; Monge, M. A. *Angew. Chem., Int. Ed.* **2006**, *45*, 7998.
(2) Geng, F. X.; Xin, H.; Matsushita, Y.; Ma, R. Z.; Tanaka, M.; Izumi, F.; Iyi, N.; Sasaki, T. *Chem.—Eur. J.* **2008**, *14*, 9255.

typical Eu^{3+} red emissions at room temperature, which confers upon them exciting potential applications in optoelectronic devices. Layered rare-earth compounds of similar stoichiometry in nitrate-forming $Ln_2(OH)_5(NO_3) \cdot xH_2O$ (Ln = Gd−Lu, Y; $x \approx 1.5$) were also presented in a recent paper, demonstrating anion exchange capability through reactions with a wide range of organic carboxylate and sulfonate anions.[3] A synergy effect by combining the advantages of a lanthanide host and anion exchangers is expected to open new avenues in the field of layered compounds and make them rather appealing for potential technological applications in such fields as luminescence, adsorbents, and catalysis. However, systematic knowledge about possible members and their behavior is still lacking. As the lanthanide series is traversed, the size of the lanthanide ions decreases monotonically. Both the crystal structure and physical properties of several lanthanide compounds demonstrated gradual variation on ascending the series as a result of lanthanide contraction.[4] Accordingly, the characteristics of this new family are likely to change with the variation in the lanthanide centers. In this regard, investigations across the series to reveal possible members and general trends in this peculiar layered family are strongly required.

In the present paper, following the successful synthesis of $Eu_8(OH)_{20}Cl_4 \cdot 6.4H_2O$, we report additional members of the $Ln_8(OH)_{20}Cl_4 \cdot nH_2O$ family with Ln = Nd, Sm, Gd, Tb, Dy, Ho, Er, Tm, and Y through a similar synthetic approach, that is, homogeneous precipitation of $LnCl_3 \cdot xH_2O$ with hexamethylenetetramine (HMT). Unusual reversible interlayer contraction/expansion was observed for certain members at a critical relative humidity by removal/absorption of coordinated water molecules. The structure of the various members of the $Ln_8(OH)_{20}Cl_4 \cdot nH_2O$ family was determined by Rietveld refinement of powder X-ray diffraction data. As the lanthanide series is traversed, the unit cell parameters, water coordination ability, and mean Ln−O distance demonstrated systematic variance with respect to the rare-earth cation size.

Experimental Section

Sample Preparation. Synthesis was conducted according to the procedures described in our previous paper.[2] All rare-earth elements (La, Ce, Pr, Nd, Sm, Gd, Tb, Dy, Ho, Er, Tm, Yb, Lu, and Y) were tested. $LnCl_3 \cdot xH_2O$ were of 99.99% purity purchased from Rare Metallic Co., Ltd. and were used as received without further treatment. Milli-Q water was used throughout. A mixture of $LnCl_3 \cdot xH_2O$ (5 mmol), NaCl (65 mmol), and HMT (5 mmol) was dissolved in 1000 cm³ Milli-Q water, and the solution was heated at refluxing temperature under continuous magnetic stirring and nitrogen gas protection. The refluxing period was usually set at 10−12 h. The obtained final products were recovered by filtration, washed with distilled water to remove any possible ionic remnants, and then dried in a box with humidity set at ∼75%.

Sample Characterization. The phase purity was examined by powder X-ray diffraction (XRD) using a Rigaku Rint ULTIMA+ diffractometer with graphite-monochromatized Cu Kα radiation (λ = 1.5405 Å) equipped with a humidity control on the sample chamber. Since the samples were very sensitive to humidity, their diffraction patterns were usually recorded at a relative humidity (RH) of 75% to preserve the high crystalline nature of the samples. In situ powder XRD patterns under various RHs typically ranging from 5% to 90% were also recorded to examine the effect of

humidity. The samples were kept at the specific humidity for 90 min before the XRD profiles were recorded. The weight change due to RH was measured at 25 °C using a Rigaku Thermo Plus TG8120 analyzer by introducing an RH-controlled N_2 atmosphere at 1 L/min. The samples were first kept in N_2 at ∼90% RH for 1−2 h until their weight was stable, and then the weight was recorded after 30 min of holding at each 10% decrease in RH. The size and morphology of the samples was examined using a JEOL JSM-6700F field emission scanning electron microscope. Transmission electron microscopy (TEM) characterization and selected-area electron diffraction (SAED) were performed employing a JEOL JEM-1010 transmission electron microscope at an accelerating voltage of 100 kV. Dispersion in ethanol was obtained by sonicating the solid sample for 10 min, after which a few drops were placed onto the TEM grid and dried for observation. Elemental analysis of the samples was carried out by inductively coupled plasma atomic emission spectroscopy (ICP-AES) on a Seiko Instruments SPS1700HVR spectrometer.[2] Fourier transform infrared (FT-IR) spectra were collected within a range of 400−4000 cm^{-1} using KBr pellets on a Varian 7000e FT-IR spectrophotometer equipped with a liquid nitrogen cooled MCT detector.

Structure Determination. High-resolution diffraction patterns for structure refinement were recorded on the BL15 at the SPring8 Synchrotron Radiation Facility, Japan. The powder samples were packed in Lindenmann capillary tubes of 0.2 mm ∅, and the data were collected under ambient conditions, using a monochromatic wavelength of λ = 0.65297 Å. The structure parameters of all samples were refined by Rietveld profile analysis using the RIETAN-FP software package.[5] The space group and initial atomic position of species assigned from previous refinement results on $Eu_8(OH)_{20}Cl_4 \cdot 6.4H_2O$,[2] as well as lattice constants calculated with an indexing program (APPLEMAN),[6] were used as initial parameters for the refinement. After the successful refinement of the lattice constants and atom positions, occupancy factors of H_2O units were consecutively added as refinable variables. Finally, the structural model, with the occupancy of the water molecules fixed, was subjected to further refinement cycles. The ultimate refined fractional atomic coordinates along with site occupancy and refinement statistics for the various $Ln_8(OH)_{20}Cl_4 \cdot nH_2O$ phases are listed in the Supporting Information.

Photophysical Characterization. Room-temperature photoluminescence was carried out using a Hitachi F-4500 fluorescence spectrophotometer.

Results and Discussion

General Synthesis and Composition Analysis of $Ln_8(OH)_{20}Cl_4 \cdot nH_2O$ (Ln = Nd−Tm and Y). The homogeneous precipitation method, which was successfully applied to the synthesis of highly crystalline $Eu(OH)_{2.5}Cl_{0.5} \cdot 0.8H_2O$,[2] has been extended to other trivalent lanthanide ions from La^{3+} to Lu^{3+} and Y^{3+}. The precipitates were observed for syntheses based on La, Ce, Pr, Nd, Sm, Gd, Tb, Dy, Ho, Er, and Y after 1 h of reaction. For Tm^{3+}, Yb^{3+}, and Lu^{3+}, the solutions only became turbid after 1 h. No precipitation occurred even after 12 h of reaction. Further hydrothermal treatment at 120 °C was needed to obtain crystalline products.

Three different phases were found under identical synthesis conditions. Only Ln^{3+} of intermediate size (Nd^{3+}, Sm^{3+}, Gd^{3+}, Tb^{3+}, Dy^{3+}, Ho^{3+}, Er^{3+}, Tm^{3+}, and Y^{3+}) yielded a layered phase of $Ln_8(OH)_{20}Cl_4 \cdot nH_2O$ similar to $Eu(OH)_{2.5}Cl_{0.5} \cdot 0.8H_2O$ (Figure 1). It is noteworthy that large Ln elements, Nd and Sm, have been incorporated into the host layer of this family for

(3) McIntyre, L. J.; Jackson, L. K.; Fogg, A. M. *Chem. Mater.* **2008**, *20*, 335.

(4) (a) Wang, X.; Li, Y. D. *Angew. Chem., Int. Ed.* **2002**, *41*, 4790. (b) Haschke, J. M. *Inorg. Chem.* **1974**, *13*, 1812. (c) Han, Z. H.; Xu, P.; Ratinac, K. R.; Lu, G. Q. *J. Cryst. Growth* **2004**, *273*, 248.

(5) (a) Izumi, F. Ikeda, T. *Mater. Sci. Forum* **2000**, *321–324*, 198. (b) Izumi, F. Momma, K. *Solid State Phenom.* **2007**, *130*, 15

(6) Appleman, D. E.; Evans, H. T.; Handwerker, D. S. *Program X-ray*; Geological Survey, U.S. Department of the Interior: Washington, DC, 1966.
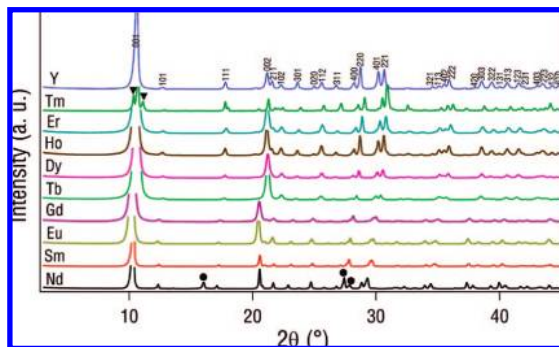
Figure 1. XRD patterns of $Ln_8(OH)_{20}Cl_4 \cdot nH_2O$ (Ln = Nd−Tm, Y). The solid circles and triangles represent impurities present in Nd^{3+} and Tm^{3+} samples, respectively.

Table 1. Elemental Analysis Results (mass %) of the As-Prepared $Ln_8(OH)_{20}Cl_4 \cdot nH_2O$ Samples

	Ln	OH	Cl	CO_3	H_2O	proposed formula
Sm	65.2	17.3	7.6	3.7	6.2	$Sm(OH)_{2.34}Cl_{0.50}(CO_3)_{0.08} \cdot 0.79H_2O$
Eu	65.5	17.7	7.5	1.27	6.1	$Eu(OH)_{2.41}Cl_{0.49}(CO_3)_{0.05} \cdot 0.78H_2O$
Gd	66.7	16.6	7.4	2.2	7.1	$Gd(OH)_{2.30}Cl_{0.49}(CO_3)_{0.10} \cdot 0.93H_2O$
Tb	67.3	17.0	7.6	1.5	6.6	$Tb(OH)_{2.36}Cl_{0.51}(CO_3)_{0.06} \cdot 0.87H_2O$
Dy	67.4	16.4	7.2	2.7	6.3	$Dy(OH)_{2.33}Cl_{0.49}(CO_3)_{0.09} \cdot 0.84H_2O$
Ho	68.3	16.9	7.3	1.6	5.9	$Ho(OH)_{2.40}Cl_{0.50}(CO_3)_{0.05} \cdot 0.79H_2O$
Er	68.3	16.7	7.2	2.3	5.5	$Er(OH)_{2.40}Cl_{0.50}(CO_3)_{0.05} \cdot 0.75H_2O$
Y	53.7	24.9	10.5	2.3	8.6	$Y(OH)_{2.42}Cl_{0.49}(CO_3)_{0.04} \cdot 0.79H_2O$

the first time, in contrast with the report on $Ln_2(OH)_5(NO_3) \cdot xH_2O$, whose members were limited to elements smaller than Gd. For Sm^{3+}-, Gd^{3+}-, Tb^{3+}-, Dy^{3+}-, Ho^{3+}-, Er^{3+}-, and Y^{3+}-based samples, almost all the diffraction peaks could be well indexed in orthorhombic symmetry identical to $Eu(OH)_{2.5}Cl_{0.5} \cdot 0.8H_2O$. An impurity phase, $Nd(OH)_3$, as marked by solid circles, was present in a small amount for Nd^{3+} whose mass percentage was determined to be about 8.1% by Rietveld analysis (vide post). For Tm^{3+}, two shoulder peaks beside the first diffraction peak, 001, are discerned by solid triangles, indicating the presence of unidentified coexisting phases. $Ln(OH)_3$ of hexagonal structure was preferred for larger Ln^{3+} (La^{3+}, Ce^{3+}, Pr^{3+}) (Supporting Information), whereas for the smaller heavy Ln^{3+} ions (Yb^{3+} and Lu^{3+}), homogeneous precipitation resulted in only a colloidal suspension. XRD results for the corresponding hydrothermal product suggest the formation of a different structure, which will be described elsewhere. The transition of yielded phases should be related to the gradual contraction of Ln^{3+} ions. All obtained samples of the desired layered phase displayed very sharp basal reflections. General *hkl* reflections were also sharp and symmetric. These features suggest the highly crystalline nature, i.e., well-ordered and regular stacking sequences, of hydroxide layers. Chemical analysis results of as-prepared pure samples (Sm−Er, Y) revealed that the compositions were in agreement with that of Eu, as shown in Table 1. The presence of carbonate ions may have arisen from their high affinity to the host layer.[7] For structural refinement, the carbonate charge was normalized to hydroxyls and simplified as $Ln_8(OH)_{20}Cl_4 \cdot nH_2O$.

The morphology and microstructure of the products was examined. SEM images of Sm^{3+} and Y^{3+} samples (Figure 2a,b)
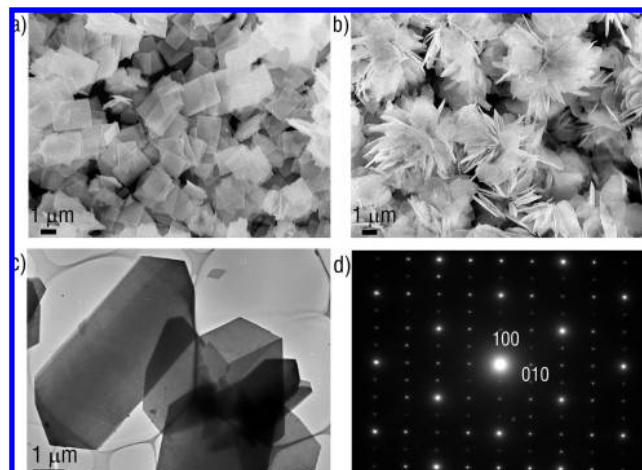
(7) (a) Miyata, S. *Clays Clay Miner.* **1983**, *31*, 305. (b) Besserguenev, A. V.; Fogg, A. M.; Francis, R. J.; Price, S. J.; O'Hare, D. *Chem. Mater.* **1997**, *9*, 241. (c) Newman, S. P.; Jones, W. *J. Solid State Chem.* **1999**, *148*, 26.

Figure 2. (a) SEM image of $Sm(OH)_{2.5}Cl_{0.5} \cdot 0.8H_2O$ showing well-developed platelets with typical dimensions of $2 \times 1 \ \mu m^2$. (b) SEM and (c) TEM images of $Y(OH)_{2.5}Cl_{0.5} \cdot 0.8H_2O$ displaying aggregates composed of high-crystallinity quasi-hexagonal platelets. (d) Corresponding SAED pattern.

are shown as examples (for other compounds, see the Supporting Information). Similar to previously reported $Eu(OH)_{2.5}Cl_{0.5} \cdot 0.8H_2O$, the Nd^{3+} and Sm^{3+} samples were crystallized into well-shaped and monodispersed rectangular platelets of $2 \times 1 \ \mu m^2$. Some nanorod-like objects were also recognized in the Nd sample and may be identified as $Nd(OH)_3$, which tends to grow in a one-dimensional morphology.[4a] However, the same refluxing process could not produce monodispersed rectangular crystals for other elements (Gd−Er and Y). For these compounds, platelet aggregates were the main product although well-developed rectangular platelets were also occasionally observed. The aggregates were dispersed in ethanol and subjected to TEM observation to further identify the morphology of the component platelets. Figure 2c shows a typical TEM image of the Y^{3+} sample. Quasi-hexagonal platelets can be clearly seen, and they show general sharp angles of 120°, which suggests that the aggregates were also composed of platelets with high crystallinity. The SAED pattern (Figure 2d) taken from an individual platelet lying on the copper grid is similar to what we reported for the Eu^{3+} case, indicating similar in-plane structure among these compounds. For the hydrothermally treated Tm sample, its morphology seemed to uniquely adopt a rhombus plate shape.

Humidity Dependence Behavior of $Ln_8(OH)_{20}Cl_4 \cdot nH_2O$ (Ln = Nd−Tm and Y). Humidity is a key factor in achieving high-crystallinity phases, because products would be either amorphous or of low crystallinity if they were overdried. Changes in the crystalline structure with humidity were studied by XRD measurements at various RHs decreasing from 90% to 5%. All gave similar crystalline phases, which suggests that no decomposition occurred (Supporting Information). Figure 3a shows changes in the basal spacing as a function of the RH.

The behavior of the series can be classified into three groups intersecting at Nd and Gd. Group I (Nd): nearly constant basal spacing as a function of the RH. The very slight and continuous decrease in the basal spacing from 8.58 to 8.55 Å should be due to water loss. Group II (Sm, Eu, Gd): two cases of discontinuous spacing of 8.5−8.6 and 8.3−8.4 Å. There was an abrupt decrease of ∼0.2 Å at critical RHs of 10%, 20%, and 50%, respectively. Group III (Tb, Dy, Ho, Er, Tm, Y): constant and smaller spacing of ∼8.3 Å. Only continuous interlayer contraction was observed, except that the spacing was smaller,
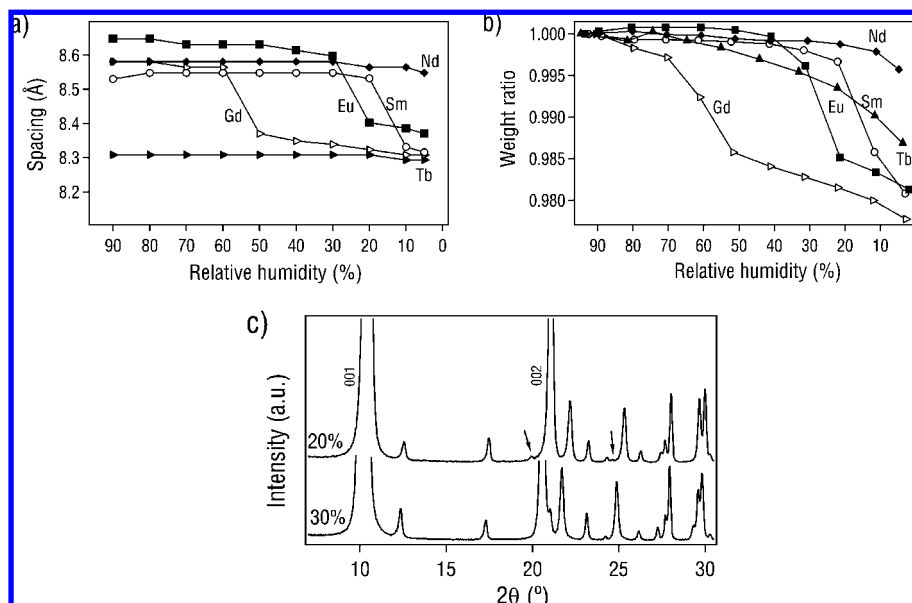
Figure 3. Changes of the (a) basal spacing and (b) weight with the relative humidity for group I (Nd), group II (Sm, Eu, and Gd), and group III (Tb as an example). (c) XRD comparison profiles of the Eu sample at RHs of 30% and 20%. The arrows indicate emergence of two additional small peaks at 20% RH.

comparable to that of group II members at low RH. Tb, as an example, decreased from 8.31 to 8.29 Å. As the abrupt shift should be correlated with different hydration states, phases before and after the shift are denoted as high-hydration (HH) and low-hydration (LH) phases, respectively.

The humidity-dependent change was confirmed by gravimetry. Weight changes, indicated in ratios relative to the weight at RH = 90%, were examined as a function of the RH values (Figure 3b). Group II (Sm, Eu, and Gd samples) showed consistent abrupt weight loss at critical values, while only a continuous decrease was observed for the others, which agreed well with the XRD observations. In contrast to group I (Nd), whose weight was nearly unchanged (0.5% decrease), group III members underwent greater weight loss (1.5%), which might have originated from the group III members being more hygroscopic. XRD profiles at the transition point were examined for the origin of the abrupt decrease. Figure 3c shows diffraction patterns of the Eu sample around the transition point, RH = 30% and 20%, revealing the emergence of two additional small peaks after the shift, as indicated by arrows. The two peaks could only be indexed in a cell involving doubling of the cell parameter, c. This may be attributable to a superstructure of ordered vacancy of H_2O sites coordinated to lanthanide centers arising from water evaporation. When the humidity was increased, both basal spacings and the mass of the HH phases for group II members were resumed without a noticeable hysteresis. The characteristic peaks of the LH phases also disappeared, which indicates the transition could be well reversed by uptake of water molecules (Supporting Information). Further repetition cycles of desorption or absorption of water molecules by adjusting RH generated the same LH−HH phase transformation.

Structure Solution of $Ln_8(OH)_{20}Cl_4 \cdot nH_2O$ (Ln = Nd−Er and Y).[8] The crystal structure and cell parameters of $Ln_8(OH)_{20}Cl_4 \cdot nH_2O$ were determined using Rietveld refinement.

(8) Because the Tm sample contained unknown impurity phases, its structure was not refined.

As the TEM study suggested that all phases were isostructural, all of them were refined in a structural model comparable to that of $Eu(OH)_{2.5}Cl_{0.5} \cdot 0.8H_2O$, isotypic with the layered structure built of $[Ln_8(OH)_{20}(H_2O)_n]^{4+}$ undulated cationic layers with chloride ions residing in the gallery. Satisfactory fitting was obtained for all the samples. The final Rietveld plots and reliability factors are provided in the Supporting Information. As Gd marks the boundary of transition from the HH phase to the LH phase, synchrotron data for both the HH and LH phases of the Gd sample were collected to make a straightforward structure comparison between the two phases. For preparing the low-hydration sample for synchrotron measurement, the sample powders were packed in a capillary tube just as usual. For the high-hydration sample, wet cotton was used to close the capillary, keeping high humidity inside.

The orthorhombic cell viewing along the c, b, and a axes is shown in Figure 4. There are three crystallographically distinct sites for Ln in the unit cell (shown as purple balls and labeled Ln1, Ln2, and Ln3), five distinct sites for hydroxyls, three for water molecules, and one unique site for chloride ions. Each hydroxyl acts as a μ_3-bridge connecting the lanthanide centers. All phases have two types of lanthanide metal environments containing 9- and 8-fold coordination. Ln1 is surrounded by seven hydroxyls and one water molecule, $\{Ln(OH)_7(H_2O)\}$, forming a dodecahedron. The second lanthanide environment for Ln2 and Ln3 has oxygen atoms bonded to eight hydroxyls and one water molecule, $\{Ln(OH)_8(H_2O)\}$, forming a mono-capped square antiprism with the capping position occupied by the water molecule. Each LnO_8 polyhedron is linked to two other LnO_8 polyhedra and four LnO_9 polyhedra via edges. These linked polyhedron units form a two-dimensional host layer parallel to the ab plane. One crystallographically unique Cl^- anion is located in the interlayer space with the $Ln \cdots Cl$ distance being about 4.5−5.0 Å depending on the lanthanide ion species, significantly longer than the bond length, for example, ~2.8 Å, for ionic interactions. This indicates that the chloride ions are accommodated in the gallery as counterions typical for anionic
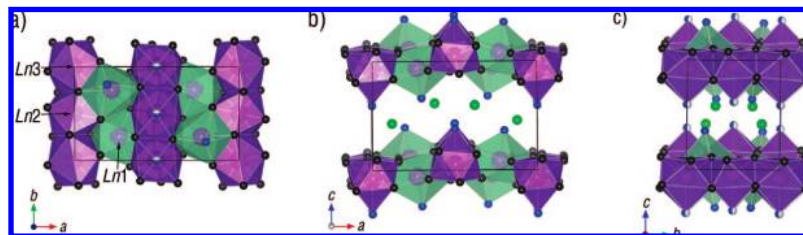
Figure 4. $Ln_8(OH)_{20}Cl_4 \cdot nH_2O$ unit cell viewed down the (a) *c* axis, (b) *b* axis, and (c) *a* axis. Ln atoms are depicted as purple balls, hydroxyls as gray balls, water molecules as blue balls, and chloride ions as green balls. The black lines represent the unit cell. The 8-fold dodecahedron polyhedron and 9-fold monocapped square antiprism are in light green and purple, respectively.
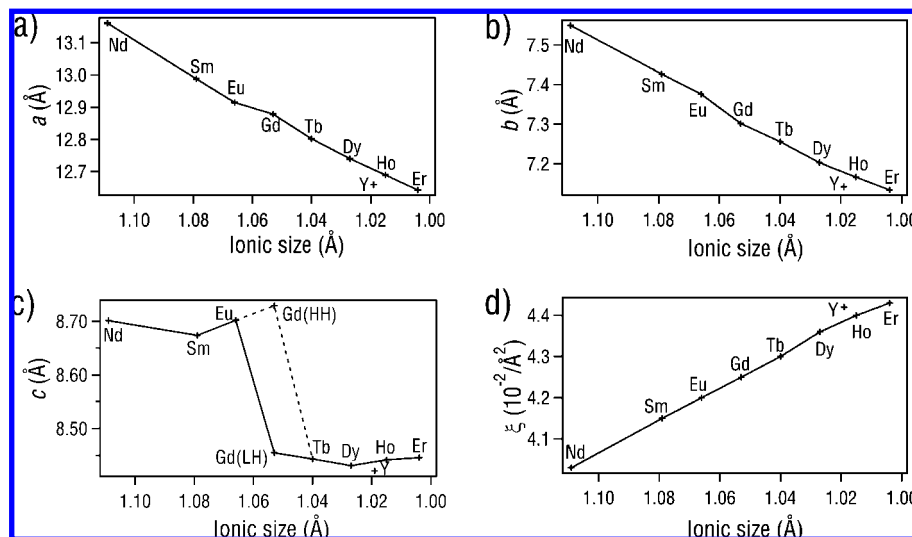

Figure 5. Correlation of the lattice parameters (a) *a*, (b) *b*, and (c) *c* and (d) layer charge density (*ξ*) with the cationic sizes. The dashed line in the graph for *c* is for the HH phase of the Gd sample.

clays, providing facile anion exchange reactions as shown in the Supporting Information.

Lattice Constant Evolution. The series of lanthanide(III) ions, in which the size decreases with increasing atomic number, provides unique possibilities for studying structural evolution trends across the series. The table of lattice parameters (space group $P2_12_12$) and unit cell volume is given in the Supporting Information along with the cation sizes for reference. Figure 5 shows the plots of the lattice constants in relation to the cation size. It can be seen that the in-plane parameters, *a* and *b*, decreased nearly monotonically with decreasing cation size/increasing atomic number. As *a* and *b* are related to the metal-to-metal distances, an increase in the rare-earth atomic number, i.e., a decrease in the cation size, accordingly resulted in a decrease in the *a* and *b* parameters. However, there was a slight cusp in the plots for both *a* and *b* at Gd^{3+} where the 4f electron shells are half-filled. If the Ln^{3+} ions have the same coordination structure, the cell volume should continuously decrease, taking the lanthanide contraction into account. However, a discontinuity was always observed at a point around the middle of the series, at Gd.[9] The most acceptable explanation might be the so-called "gadolinium break" effect, which is related to the half-filled 4f shell of Gd.

The interlayer distance or *c* for Nd^{3+}, Sm^{3+}, and Eu^{3+} was nearly the same at ~8.70 Å, whereas that for Tb^{3+}, Dy^{3+}, Ho^{3+},

Er^{3+}, and Y^{3+} was ~8.45 Å. HH Gd^{3+} and LH Gd^{3+} were comparable to the former and the latter, respectively. This phenomenon can be well understood by the difference in the hydration behavior of the compounds described above.

Lanthanide Hydration (Water Deficiency) in Crystal Structures. The change in hydration state from Gd is also supported by the refinement results, which may provide more clues about the phase stability associated with the hydration behavior. Refinement of the site occupancy factors in all cases resulted in full occupancy of water in dodecahedron $\{Ln(OH)_7(H_2O)\}$, while all showed reduced occupancy of the capping position in the monocapped square antiprism $\{Ln(OH)_8(H_2O)\}$ that could originate from repulsion between the oxygen atoms of the prism and the capping water molecules. Hydration numbers of $Ln_8(OH)_{20}(H_2O)_nCl_4$ obtained from refinement together with those from chemical analysis are provided in Table 2. The hydration numbers obtained are somewhat correlated to the interlamellar spacing. While the number of water molecules in the HH phases is generally more than 6.0 with a spacing of ~8.65 Å, the hydrated number for the LH phases is less than 6.0 with a smaller spacing of ~8.45 Å. The total occupancy of the three sites generally decreased with increasing atomic number both for HH phases from Nd to Gd except Sm (Nd, 7.4; Sm, 6.3; Eu, 7.2; Gd, 6.6) and for LH phases from Gd to Er (Gd, 6.0; Tb, 5.8; Dy, 5.6; Ho, 5.4; Er, 4.9). This could be ascribed to the fact that the above-mentioned repulsion from neighboring oxygen atoms might increase with decreasing size of the central lanthanide

(9) (a) Beall, G. W.; Milligan, W. O.; Wolcott, H. A. *J. Inorg. Nucl. Chem.* **1977**, *39*, 65. (b) Johnson, D. A. *Some Thermodynamic Aspects of Inorganic Chemistry*, 2nd ed.; Cambridge University Press: Cambridge, U.K., 1982.

Table 2. Site Occupancy Factors and Number of Water Molecules from Refinement and Chemical Analysis (CA)

Ln	occupancy, H$_2$O(2)/H$_2$O(3)	water number from refinement	water number from CA
Nd	0.98/0.72	7.4	a
Sm	0.58/0.55	6.3	6.3
Eu	0.91/0.69	7.2	6.2
Gd	HH, 0.73/0.58; LH, 0.61/0.37	HH, 6.6; LH, 6.0	7.4
Tb	0.36/0.54	5.8	7.0
Dy	0.50/0.30	5.6	6.7
Ho	0.33/0.36	5.4	6.3
Er	0.24/0.21	4.9	6.0
Y	0.47/0.71	6.4	6.3

^{a} The presence of an impurity phase, Nd(OH)$_3$, prevented accurate analysis.

ions.[10] A recent study on [Ln(H$_2$O)$_n$](CF$_3$SO$_3$)$_3$ revealed a similar tendency in which water deficiency started at Ho and increased with increasing atomic number.[11] Chemical analysis results showed a similar trend, although there was some discrepancy between the refinement and experimental results. The discrepancy may be due to the presence of additional water molecules adsorbed on the surface or possible water evaporation before or during synchrotron measurement. As all the coordinated water molecules are pointing toward the interlayer spaces, they appear to have an important role in stabilizing the layered structure. Loss of coordinated water molecules resulted in abrupt layer contraction, as supported by studies on humidity dependence behavior described above. Furthermore, the decrease in coordinated water molecules with an increase in the atomic number makes the LH phase more preferred, and Er is the limit for phase stability of a layered structure where the hydration number in each monocapped square antiprism was only about 0.4. Even though synthesis was performed in the same aqueous media for Yb and Lu, the square antiprism might eventually become water-free considering the combined effect of the smaller effective ionic radii and the increased repulsion; consequently, the layered structure could not be retained.

Ln–O Average Distance. To determine the evolutional trend of the Ln–O bond length with increasing atomic number of Ln, the Ln–O distance was examined. The coordination shells for Ln1 and Ln2/Ln3 are in point groups of C_1 and C_{4v} with eight and five independent Ln–O bond distances, respectively. The bond length for each Ln site was averaged for estimation purposes. The average observed Ln–O bond distances with those calculated using the Shannon radii are listed in a table provided in the Supporting Information. Figure 6 plots the average Ln–O bond lengths as a function of the ionic radius of the rare-earth ions for the three independent sites. In general, the average Ln2–O and Ln3–O distances were longer than that for Ln1–O. This is reasonable since Ln2 and Ln3 have a higher coordination number than Ln1. It should be noted that the distance does not vary smoothly with the ionic radius. For Ln1, the water position was fully occupied for all cases and the mean Ln–O distance decreased with decreasing ion radius from Nd to Eu and from Gd to Er. However, there was an increase from Er to Gd as the gadolinium break proposes. As the occupancy of water coordinated to Ln2 and Ln3 kept changing across the series, the Ln2–O and Ln3–O distances were more or less

influenced by the occupancy of water, and only some members fell on a decreasing line. It is also worth noting that the heavy end member Er exhibited almost equivalent mean Er–O distances for all three sites, and the practical coordination numbers for the two sites of 9-fold coordination became 8.46 and 8.42, respectively. This suggests that the Er coordination sphere was crowded enough and there might be a structure–stability limit based on the size of the lanthanide ions. Er^{3+} represents the lower limit of stability, and the further heavier (smaller) lanthanide members, including Yb and Lu, cannot retain the analogous layered structure because of their considerably smaller ionic size and possible lower coordination number which results in a different phase. Nd^{3+} roughly represents the upper limit of stability because it was the largest cation successfully incorporated into this structure. These results are reminiscent of the same synthesis conditions that resulted in Ln(OH)$_3$ (La, Ce, Pr), in which the lanthanide center is coordinated to nine hydroxyls.[12] It is interesting that the metal coordination number of the yielded compounds steadily decreases from only 9 (La, Ce, Pr) to 9 and 8 (Nd, Sm, Eu, Gd, Tb, Dy, Ho, Er, Tm) and possibly 8 or smaller (Yb, Lu), which is associated with lanthanide contraction.

Y^{3+} is much lighter in weight than the lanthanide ions, but all studies showed that the Y sample exhibited characteristics analogous to those of lanthanide ions. This correlates with its similar 4f shell structure and ionic radius very close to that of lanthanide ions, lying between those of Dy^{3+} and Ho^{3+}.

Photoluminescence Study of Tb$_8$(OH)$_{20}$Cl$_4$·7.0H$_2$O. The study of the photoluminescent properties of the Tb^{3+}-based sample and observation of typical Tb^{3+} green emission suggest that it may hold great potential in high-performance luminescent devices. Room-temperature excitation and emission spectra of Tb$_8$(OH)$_{20}$Cl$_4$·7.0H$_2$O are shown in Figure 7, where the excitation spectra were obtained by monitoring at 545 nm and the emission spectra were measured using an excitation wavelength of 354 nm. The excitation spectrum monitored within the intra-4f^8 ^{5}D$_4$–^{7}F$_5$ emission lines was formed of two UV broad bands at approximately 230 and 250 nm superimposed on a series of Tb^{3+} straight lines. The two UV broad bands can be assigned to the spin-allowed (low-spin, LS) and spin-forbidden (high-spin, HS) interconfigurational Tb^{3+} fd transitions.[13] When the compound was excited into the UV band or directly into the intra-4f^8 levels, emission peaks from 400 to 800 nm were identified as corresponding to ^{5}D$_4$–^{7}F$_J$ ($J = 3–6$) transitions of the Tb^{3+} ion: 484 nm (^{5}D$_4$–^{7}F$_6$), 543 nm (^{5}D$_4$–^{7}F$_5$), 589 nm (^{5}D$_4$–^{7}F$_4$), and 626 nm (^{5}D$_4$–^{7}F$_3$). The ^{5}D$_4$–^{7}F$_5$ emission was the strongest in the investigated range, indicating that Tb$_8$(OH)$_{20}$Cl$_4$·7.0H$_2$O has typical Tb^{3+} green light emission. The splitting of ^{5}D$_4$–^{7}F$_6$ and the presence of shoulder peaks beside the emission peak ^{5}D$_4$–^{7}F$_{4,5}$ may have been caused by the low-symmetry coordination environment. No emission was detected in the ^{5}D$_3$–^{7}F$_J$ spectral region because of the high concentration of Tb^{3+}.[14]

Conclusions

We have demonstrated that nine new layered rare-earth hydroxides with a composition of Ln$_8$(OH)$_{20}$Cl$_4$·nH$_2$O (Ln =

(10) Abbasi, A.; Lindqvist-Reis, P.; Eriksson, L.; Sandström, D.; Lidin, S.; Persson, I.; Sandström, M. *Chem.–Eur. J.* **2005**, *11*, 4065.

(11) Persson, I.; D'Angelo, P.; De Panfilis, S.; Sandström, M.; Eriksson, L. *Chem.–Eur. J.* **2008**, *14*, 3056.

(12) Zachariasen, W. H. *Acta Crystallogr.* **1948**, *1*, 265.

(13) van Pieterson, L.; Reid, M. F.; Wegh, R. T.; Soverna, S.; Meijerink, A. *Phys. Rev. B* **2002**, *65*, 045113.

(14) Bazzi, R.; Flores-Gonzalez, M. A.; Louis, C.; Lebbou, K.; Dujardin, C.; Brenier, A.; Zhang, W.; Tillement, O.; Bernstein, E.; Perriat, P. *J. Lumin.* **2003**, *102*, 445.
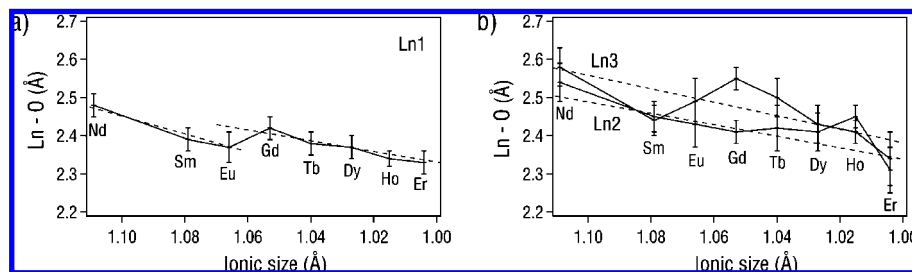
Figure 6. Correlation of bond lengths (a) Ln1−O and (b) Ln2−O and Ln3−O with ionic size. The dashed lines represent the trends shown by the data.
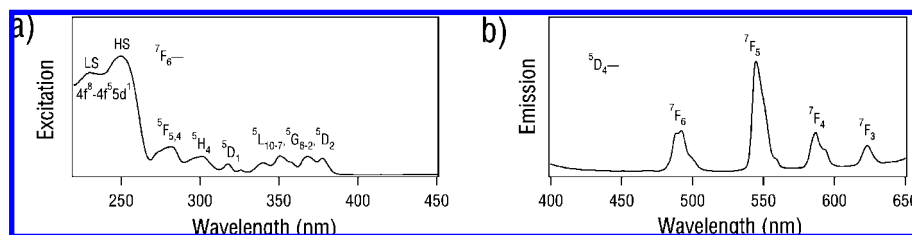

Figure 7. Room-temperature (a) excitation and (b) emission spectra of $Tb(OH)_{2.5}Cl_{0.5} \cdot 0.9H_2O$ monitored around 545 nm and excited at 354 nm.

Nd, Sm, Gd, Tb, Dy, Ho, Er, Tm, and Y) can be formed through homogeneous precipitation of $LnCl_3 \cdot xH_2O$ with HMT. All phases are of high crystallinity and are well developed, but they are very sensitive to humidity conditions. The "lanthanide contraction" is important. Larger lanthanides, $Nd_8(OH)_{20}Cl_4 \cdot 7.4H_2O$, and smaller lanthanides, $Ln_8(OH)_{20}Cl_4 \cdot nH_2O$ (Ln = Tb−Tm, Y) adopt HH and LH phases, respectively, throughout the humidity range of 5−90%. Sm, Eu, and Gd samples exhibited an RH-induced reversible basal shift between the HH and LH phases as large as ∼0.2 Å at critical RHs of 10%, 20%, and 50%. All the structures were successfully refined in an isostructural orthorhombic series with two different coordination environments: 8-fold, coordinated in a dodecahedron, and 9-fold, forming a monocapped square antiprism. Both Ln^{3+} centers have a water coordination pointing toward the gallery, and the coordinated water molecules play a critical role in stabilizing the layered structure. Crystallographic refinement of occupancy factors revealed that water in the former is fully occupied, whereas the capping water is deficient in the latter due to repulsion from the prism oxygen atoms. The deficiency increases with an increase in the atomic number; consequently, the low-hydration phase becomes more preferred for heavier lanthanides, with the total hydration number per cell being 7.4, 6.3, 7.2, and 6.6 for high-hydration Nd, Sm Eu, and Gd and 6.0, 5.8, 5.6, 5.4, and 4.9 for low-hydration Gd, Tb, Dy, Ho, and Er. Also, Er is the stability limit for the layered structure, with the water molecule decreasing to only ∼0.4 in each monocapped square antiprism. Examination of structural trends as a function of the size of the lanthanide centers revealed the importance of the gadolinium break effect because an abrupt and concomitant transition occurs at Gd in both the lattice parameters and mean bond distance. Photoluminescence studies of the Tb^{3+}-based sample showed typical Tb^{3+} green emission that may hold great potential in high-performance luminescent devices. The layered structure, typical of anionic clays, imparts unique anion exchangeability to the compounds; coupled with lanthanide host layers serving as useful phosphors, they become promising candidates for applications in a number of areas such as nanocomposites, catalysis, and optoelectric devices.

Supporting Information Available: Refined atom positions, occupancy factors, and refinement statistics, XRD and SEM images of $Ln(OH)_3$ for La, Ce, and Pr, more SEM images, XRD profiles vs RH, reversible humidity-triggered basal spacing/mass change, RIETAN fitting patterns, anion-exchange reactions, and tables of unit cell dimensions and mean Ln−O distances. This material is available free of charge via the Internet at http://pubs.acs.org.

JA807050E